Auto-passivation of crystal defects in hybrid imidazolium/methylammonium lead iodide films by fumigation with methylamine affords high efficiency perovskite solar cells

Yi Zhang,[a,b] Giulia Grancini,[a] Zhaofu Fei,[a,*] Erfan Shirzadi,[a] Xuehui Liu,[b] Emad Oveisi,[c] Farzaneh Fadaei Tirani,[a] Rosario Scopelliti,[a] Yaqing Feng,[b] Mohammad Khaja Nazeeruddin[a,*] and Paul J. Dyson,[a,*]

[a] *Institut des Sciences et Ingénierie Chimiques, Ecole Polytechnique Fédérale de Lausanne (EPFL), CH-1015 Lausanne, Switzerland.*

[b] *School of Chemical Engineering and Technology, Tianjin University, Tianjin 300072, China.*

[c] *Interdisciplinary Centre for Electron Microscopy, Ecole Polytechnique Fédérale de Lausanne, CH-1015 Lausanne, Switzerland.*

E-mail: zhaofu.fei@epfl.ch, mdkhaja.nazeeruddin@epfl.ch, paul.dyson@epfl.ch

Abstract: Hybrid perovskite solar cells have attracted tremendous interest in the photovoltaic community. Despite their high defect tolerance, reducing the trap density by material engineering and surface modification is still critical to further boost performance. Here, methylammonium lead(II) iodide perovskite has been doped with imidazolium iodide in high concentrations (10 – 30 mol%) to boost solar cell performance, by passivating defects. Fumigation with methylamine results in the deprotonation of the embedded imidazolium cations, generating imidazole and methylammonium cations. The resulting (neutral) imidazole is extruded from the 3-D perovskite crystal and distributes around the crystal leading to auto-passivation of crystal defects. The structure of the imidazolium-PbI_3 salt intermediate (i.e. formed in the absence of the methylammonium cation) has been determined and the resulting perovskite film characterized. Employed in solar cells, a power conversion efficiency (PCE) up to 20.14% is demonstrated.

Keyword: Perovskite solar cells, Methylammonium lead iodide, Passivation of crystal defects, Fumigation, imidazolium-PbI_3 salt

Introduction

In recent years the performance of perovskite-based solar cells (PSCs) has improved considerably,[1,2,3,4] with the most widely used light absorber comprising methylammonium lead triiodide ($MAPbI_3$) combined with other cations.[5,6,7,8] To boost device efficiency compositional engineering by incorporating mixed cations such as Cs^+ or Rb^+ has been the most explored route. [9] However, increasing the control on the quality of the perovskite layer[10,11] and of the interfaces between the perovskite layer and the electron transport layer (ETL),[12,13] and hole transport layer (HTL),[14,15] are of crucial importance. In recent years, to improve the quality of the perovskite layers, several techniques have been applied, including healing the defects of the perovskite layers through

chemical passivation. As an example, an excess of PbI_2 in nonstoichiometric precursor solution has been shown to increase the device PCE resulting in a reduced defect density compared to that of stoichiometric reference cell.[16,17] Extending this approach, different compounds (including salts) have been used to adjust the defects and interfaces of perovskite layer. Examples include passivation with Lewis bases that stabilize under-coordinated Pb(II) ions, [18] and iodopentafluorobenzene, which coats the perovskite forming halogen bonding donor-acceptor interactions.[19] An amine-based polymer has been also used as a surfactant to promote uniform crystallization, while passivating the $MAPbI_3$ and assisting the growth of a more uniform distribution of crystals, leading to improved open circuit voltages.[20] Most recently, quaternary ammonium halides have been used for the passivation of perovskite films resulting in enhanced PSC.[17] However, almost all these compounds have been directly mixed within the perovskite precursor solution, affecting the growth of perovskite crystals. The use of additives not only plays an important role in passivating defects, but also in improving the interfacial interactions with the ETLs and/or HTLs, which ultimately results in improved PCEs, [21,22,23] as well as modulating the crystal growth and overall film surfaces.[24,25] In order to improve interface interactions, fumigation of pre-formed perovskite films with gaseous methylamine, as a post-treatment, has been also proposed as a way to improve the quality of perovskite surfaces enhancing the interactions between the perovskite layers and the HTL.[26]

Here, we describe the use of high concentrations of imidazolium iodide as a doped co-reactant for the fabrication of perovskite films, followed by fumigation with gaseous methylamine. This second step further fine-tunes the quality of the perovskite film and, due to the stronger basicity of methylamine compared to imidazole,[27,28] resulting in the deprotonation of the imidazolium cation in the perovskite film which releases imidazole (IMD). The released IMD distributes around the crystal edges, leading to auto- passivation of crystal defects. Using this approach, a PSC with a PCE of 20.14% was obtained as measured at standard AM 1.5.

Results and discussion

High concentrations of IMI were included in the preparation of $MAPbI_3$ perovskite films, i.e. 10, 20 or 30 mol% IMI relative to MAI and PbI_2 (0.9:1, 0.8:1 or 0.7:1 ratio) in DMSO, to afford films of formula $IM_{0.1}MA_{0.9}PbI_3$, $IM_{0.2}MA_{0.8}PbI_3$ and $IM_{0.3}MA_{0.7}PbI_3$. As controls, films of pure $MAPbI_3$ and $IMPbI_3$ were also prepared from dimethyl sulfoxide (DMSO). The resulting films were obtained by spin-coating onto FTO glass and fumigation with methylamine gas (see Experimental for full details). Both the untreated and fumigated films were characterized by X-ray diffraction (XRD, Figure 1).

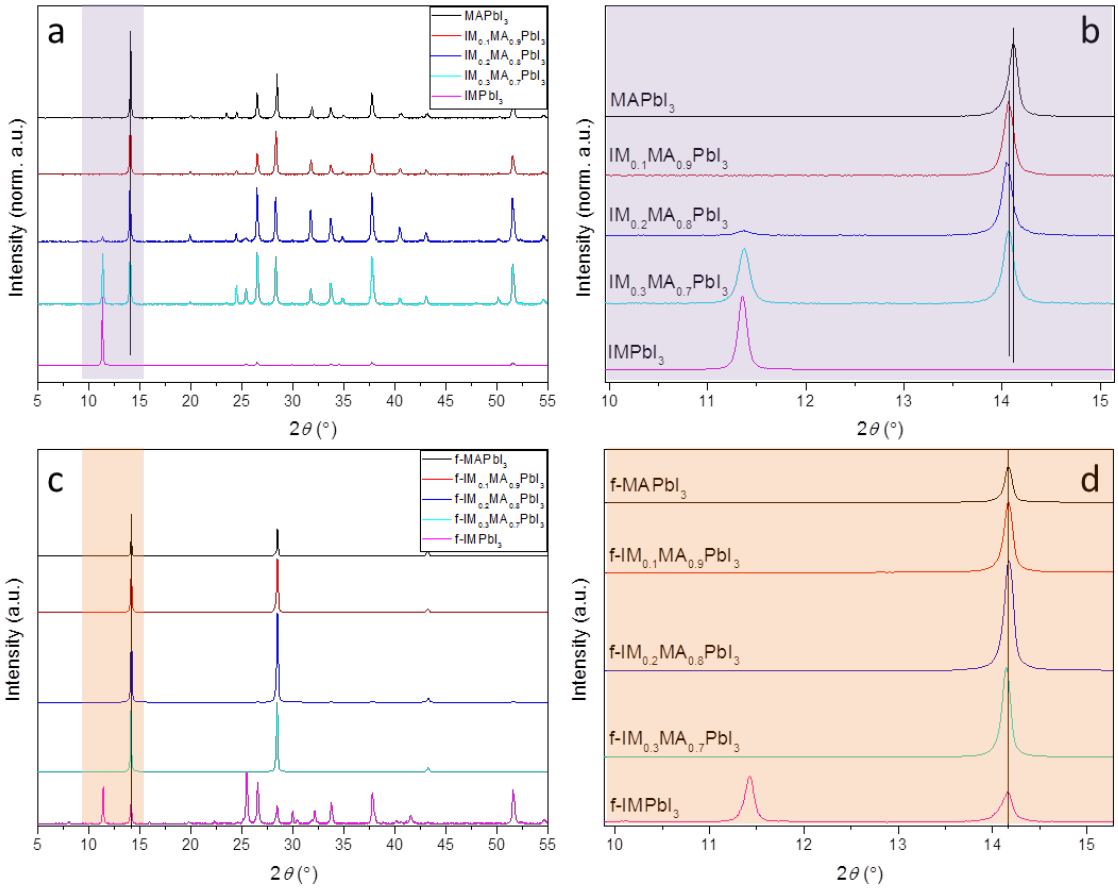

Figure 1. X-ray diffraction (XRD) patterns of (a) the spin-coated $MAPbI_3$, $IM_{0.1}MA_{0.9}PbI_3$, $IM_{0.2}MA_{0.8}PbI_3$, $IM_{0.3}MA_{0.7}PbI_3$ and $IMPbI_3$ perovskite films (before fumigation) and (b) highlighted diffraction profiles in the range from *2Θ* 10° to *2Θ* 15°, (c) methylamine gas fumigated perovskite films f-$MAPbI_3$, f-$IM_{0.1}MA_{0.9}PbI_3$, f-$IM_{0.2}MA_{0.8}PbI_3$, f-$IM_{0.3}MA_{0.7}PbI_3$ and f-$IMPbI_3$ and (d) highlighted diffraction profiles in the range from *2Θ* 10° to *2Θ* 15° of the fumigated films.

Figure 1a shows the XRD patterns of the spin-coated (non-fumigated) perovskite films $IMPbI_3$, $IM_{0.1}MA_{0.9}PbI_3$, $IM_{0.2}MA_{0.8}PbI_3$ and $IM_{0.3}MA_{0.7}PbI_3$ and pure $IMPbI_3$, in the region between 10° to 15° (expanded in Figure 1b). The pure $IMPbI_3$ film shows a peak at 11.34°, i.e. in a similar position to that observed for the δ-$FAPbI_3$ phase, [29,30,31] which can be assigned to the (110) peak of a 1-dimensional phase (note that the single crystal X-ray structure of $IMPbI_3$ has been determined and confirms this structure – see below). Indeed, it is important to mention that due to the limit set by the Goldschmidt tolerance factor rule, only the cations with an active radius < 2.56 Å can be incorporated and centred inside the three-dimensional perovskite structures within the octahedral PbI_6 cages, thus limiting the choice according to the dimensions of the cation. Other cations, such as guanidium (GA), alkylammonium or alkyl imidazolium, being larger in size then the empirical limit, are indeed unable to fit inside the PbI_6 cages of the perovskite structures, leading to the collapse of the three-dimensional network, or forming lower dimensional perovskites.[32] However, despite the slightly larger dimensions, it has been predicted and recently demonstrated that even larger cations such as GA and imidazolium (IM) can be incorporated into the octahedral PbI_6 cages when mixed in small amount with MA,

keeping a stable three-dimensional perovskite structures.[33,34] This is valid only if a certain percentage of GA is added together with MA (up to 15%).[35] Beyond that, phase segregation occurs and pure GA-based perovskite forms two or one-dimensional perovskite phase.[35] Although the effective radii of the imidazolium cation (2.58 Å) is only marginally larger than that of the formamidinium (2.53Å) which forms three-dimensional structures,[36] the reaction of pure imidazolium iodide (IMI)[37] with PbI_2 leads to the formation of imidazolium lead triiodide ($IMPbI_3$) arranging into a one-dimensional structure.[38] The XRD pattern of the film containing 10% IMI, i.e. $IM_{0.1}MA_{0.9}PbI_3$, does not contain the peak at 11.34°, instead a peak at 14.06° is observed similar to that of the pure untreated $MAPbI_3$ film (at 14.15°), but slightly shifted when compared to pure $MAPbI_3$, suggesting that the structure of $IM_{0.1}MA_{0.9}PbI_3$ comprises of a typical 3-dimensional orthorhombic perovskite phase. The calculated *d-spacing* of the perovskite crystal unit changes from 6.28 Å in $MAPbI_3$ to 6.32 Å $IM_{0.1}MA_{0.9}PbI_3$, indicating that partial replacement of the MA cation by the larger IM cation decreases the tolerance factor.[39,40,41] The incorporation of a comparatively large cation into a 3-dimensional perovskite structure can lead to the observed lattice expansion, which at 10% IMI is counter-balanced by the small MA cation,[42,43,44] thus stabilizing the 3-dimensional network, as in the case of the incorporation of GA.[35,41,45] However, as the amount of IMI in the film increases beyond 10%, i.e. in the $IM_{0.2}MA_{0.8}PbI_3$ and $IM_{0.3}MA_{0.7}PbI_3$ films, diffraction peaks at 11.34° presumably corresponding 1-dimensional $IMPbI_3$ structures appear, indicating that lattice expansion is not unlimited. Thus, the $IM_{0.2}MA_{0.8}PbI_3$ and $IM_{0.3}MA_{0.7}PbI_3$ films comprise a mixture of 3- and 1-dimensional crystals. Upon the exposure of these films to methylamine gas, the film turns into transparency and rapidly becomes black (see Supporting Information, SI). The XRD FWHM of fumigated samples, compared to spin-coated films, are all decreased (see Table S2, SI), which means the crystallinity of perovskite increases after fumigation. Given that the pK_b (base dissociation constant) of methylamine is 3.24 whereas the pK_b of imidazole is around 7,[36] exposure of the $IM_xMA_{1-x}PbI_3$ films to methylamine results in the deprotonation of IM cations and the concomitant formation of MA cations, releasing neutral IMD (Eqn. 1):

$$IMPbI_3 + CH_3NH_2(gas) \rightarrow MAPbI_3 + IMD \qquad \text{Eqn. 1}$$

In a control experiment, $IMPbI_3$ was reacted with excess methylamine in ethanol to yield $MAPbI_3$ and IMD, as evidenced by ^1H NMR spectroscopy (Figure S1-S3). When the $MAPbI_3$ was treated with methylamine solution in ethanol, an exothermic process took place spontaneously. After evaporation of the solvent and extraction of the remaining solid with diethyl ether, white crystalline imidazole can be obtained after removal of the diethyl ether. The isolated imidazole shows identical pattern in the

1H NMR spectrum in $CDCl_3$ compared with that of commercial sample (Acros) (Figure S1 and S2). Both isolated and commercial imidazole samples melt at 86-88°C. The remaining solid after washing with diethyl ether corresponds to only methylammonium lead iodide $MAIPbI_3$ (as revealed by the ^1H NMR spectrum in Figure S3). Figure 1c shows the XRD patterns of the methylamine gas fumigated films f-$MAPbI_3$, f-$IM_{0.1}MA_{0.9}PbI_3$, f-$IM_{0.2}MA_{0.8}PbI_3$, f-$IM_{0.3}MA_{0.7}PbI_3$ and f-$IMPbI_3$ in the region between 10° to 15° (expanded in Figure 1d). The (110) diffraction peak of all the films is very close to that of the $MAPbI_3$ perovskite film (2Θ ~14.15°). Notably, the peak at 11.34° in the $IM_{0.2}MA_{0.8}PbI_3$ and $IM_{0.3}MA_{0.7}PbI_3$ films prior to fumigation, is no longer present following fumigation. Since IMD is a solid at room temperature, it remains present in the perovskite film, presumably in the grains and boundaries due to its planar structure. Only the fumigated film f-$IMPbI_3$ contains peaks at both 11.34 and 14.15°, indicative of a mixture of 3- and 1-dimensional crystals, suggesting that major structural changes can take place during the reaction of the solid film with the methylamine gas at a short time (2 s).

The single crystal X-ray structure of $IMPbI_3$ was determined at 100(2) K confirming the 1-dimensional structure established by XRD analysis (see Experimental for details of crystal growth and data collection/treatment and Table S1 in supporting information). In contrast to $MAPbI_3$, which has a small unit cell of high symmetry, $IMPbI_3$ crystallizes in a hexagonal crystal system and the 1-dimensional polymer is composed of infinite $[PbI_3^+]_n$ chains (Figure 2a). The closest distances between the I-atoms between the $[PbI_3^+]_n$ chains is 4.332(4) Å (Figure 2b). This value lies in the lower end of 1-dimensional ammonium or imidazolium lead iodide complexes (usually > 5 Å).[46,47,48] Even the second shortest I···I distance of 4.613(4) Å is much shorter than that usually found in structurally related complexes. Other parameters including the Pb-I distances (ca. 3.2 Å), I-Pb-I angles around the octahedra (ca. 86-94°) and the Pb···Pb distance within the 1-dimensional chain (4.019(2) and 3.949(2) Å for Pb1 and 4.046(3) and 3.922(3) Å for Pb2) are essentially as expected.

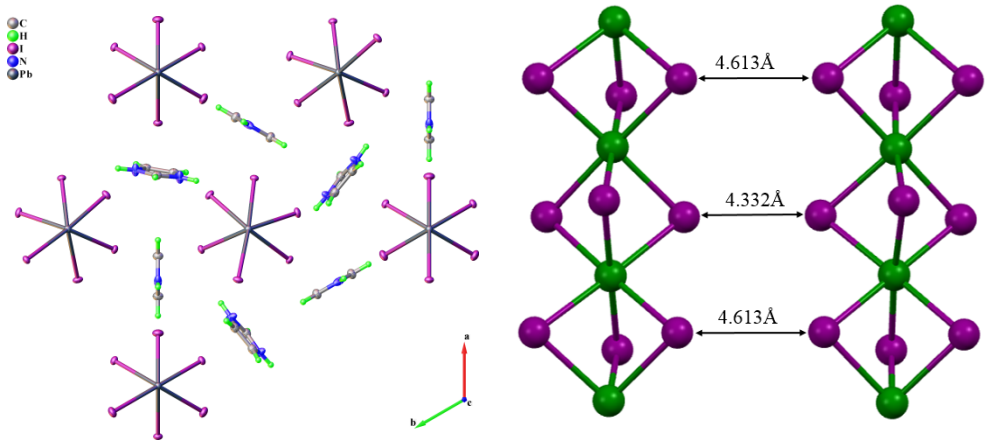

Figure 2: Packing image including the imidazolium cation (left) of $IMPbI_3$ in the solid state and the infinite $[PbI_3^+]_n$ chains highlighting the interchain I-I distances (right).

The films were further investigated using UV-Vis absorption, continuous wave photoluminescence (CWPL) and time resolved photoluminescence (TRPL) spectroscopy. Figure 3a shows the UV-Vis absorption spectra of the films before fumigation. A film of 10% IMD-doped $MAPbI_3$, termed $IMD_{0.1}MA_{1.0}PbI_3$ (molar ratio of IMD: MAI: PbI_2 = 0.1:1.0:1.0), was also studied as a control, and compared to the pure $MAPbI_3$. The absorption onset of the imidazolium-doped films decreases from $IM_{0.1}MA_{0.9}PbI_3$ to $IM_{0.3}MA_{0.7}PbI_3$, which may be due to a slight distortion of the crystal lattice, as observed by the XRD (Figure 3a). The peak position of the normalized PL spectra is also slightly shifted which, again, might due to the different crystal size in these doped films with respect to $MAPbI_3$, in agreement with the absorption shift.[49,50]

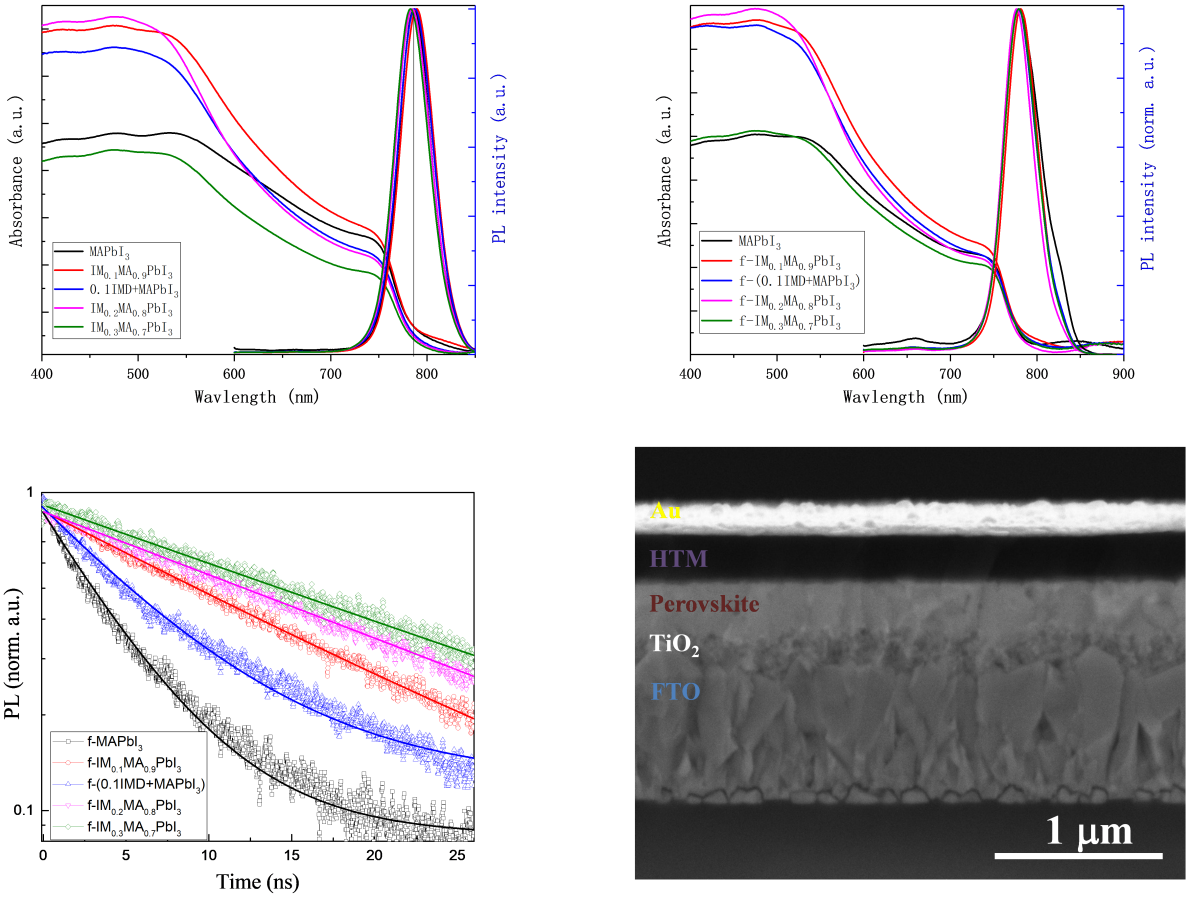

Figure 3. (a) UV-Vis absorption spectra (left) and normalized CWPL spectra (right) excited at 480 nm of spin-coated raw $MAPbI_3$, $IM_{0.1}MA_{0.9}PbI_3$, $IM_{0.2}MA_{0.8}PbI_3$, $IM_{0.3}MA_{0.7}PbI_3$ and 10% IMD doped $MAPbI_3$ films (termed $IMD_{0.1}MA_{1.0}PbI_3$), (b) UV-Vis absorption spectra (left) and normalized CWPL (right) excited at 480 nm of methylamine fumigated 10% IMD doped $MAPbI_3$ film (named as f-$IMD_{0.1}MA_{1.0}PbI_3$) and f-$MAPbI_3$, f-$IM_{0.1}MA_{0.9}PbI_3$, f-$IM_{0.2}MA_{0.8}PbI_3$, f-$IM_{0.3}MA_{0.7}PbI_3$ and f-$IMPbI_3$. (c) TRPL decay of methylamine fumigated samples excited at 480 nm at excitation density of <1 nJ cm^{-2}. The films were spin-coated on the glass and encapsulated in pmma to prevent degradation or any oxygen/moisture induced effects. (d) Cross-section SEM image of a f-$IM_{0.1}MA_{0.9}PbI_3$ film embedded within a FTO/c-TiO_2/mp-TiO_2/f-$IM_{0.1}MA_{0.9}PbI_3$/Spiro-OMeTAD/Au PSC.

Overall, we can conclude from the optical data that, following fumigation of the films with methylamine, the absorption onset and thus the bandgap, remains unchanged. As discussed above, during the fumigation process, the stronger methylamine base deprotonates the IM in the film to release neutral IMD (Eqn. 1). The normalized PL spectra also remain essentially unchanged, showing the main emission peak at about 780 nm, see Figure 3b, corroborating the mechanism described above. Dynamical radiative decay was monitored by TRPL (Figure 3c). Measurements were performed using time-correlated single photon counting (TCSPC) under low-intensity pulsed excitation at 480 nm at < nJ cm^{-2}. In this regime, the decay processes fit well with mono-exponential profiles. This does not correlate to a precise physical process, however, being the carrier density as low as $10^{14}/cm^3$, we can infer that it mainly reflects a trap-mediated recombination process, as already demonstrated.[7,15,23] Within this time window, the measurements show that the carrier lifetime of the perovskite films is longer for the fumigated IMI-doped films compared to the reference film, i.e. pure $MAPbI_3$. Being in a regime where trap filling is the dominating mechanism, this observation could be due, among other mechanisms, to a reduced recombination caused by a reduction of the trap density (passivation of defects). The retrieved lifetime of the f-$IM_{0.1}MA_{0.9}PbI_3$ film (15.73 ns) extends beyond the temporal window, and is more than three times of that of the reference cell (4.79 ns). As the concentration of IMI increases in the films the retrieved lifetime increases, i.e. for the f-$IM_{0.2}MA_{0.8}PbI_3$ and f-$IM_{0.3}MA_{0.7}PbI_3$ films the lifetimes are 22.17 and 23.25 ns, respectively (Figure 3c, Table S3, SI). However, as mentioned above, this only indicated a longer PL emission, but it does not pretend to univocally determine the photophysical parameters which would require a much more detailed investigation on the monomolecular and bimolecular processes.[51]

As mentioned above, prior to fumigation, only the $IM_{0.1}MA_{0.9}PbI_3$ film has a complete 3-dimensional structure. In the $IM_{0.2}MA_{0.8}PbI_3$ and $IM_{0.3}MA_{0.7}PbI_3$ films not all the IM cations are included in the 3-dimensional perovskite structure and the presence of a 1-dimensional phase is observed. The passivation process results in the replacement of IM cations by MA cations according to the mechanism described in Eqn. 1, but to a lesser extent than in the 3-dimensional phase (based on a comparison of the XRD patterns of the various films before and after fumigation).

Cross-section scanning electron microscopy (SEM) of the fumigated f-$IM_{0.1}MA_{0.9}PbI_3$ film embedded within a FTO/c-TiO_2/mp-TiO_2/f-$IM_{0.1}MA_{0.9}PbI_3$/Spiro-OMeTAD/Au PSC (Figure 3d, see SI for further details) reveals the total thickness of the capping and mesoporous layers to be about 520 nm (about 300 nm and 220 nm, respectively). The Spiro-OMeTAD based HTM has a thickness of 260 nm. Notably, the perovskite/HTM surface of this film is very smooth due to the natural advantages of fumigation methods. According to recent reports,[52-55] defects in the perovskite and HTM/ETM surface is the most important factor influencing the overall cell performance. The

smoother surface of the f-$IM_{0.1}MA_{0.9}PbI_3$ film results in a smaller contact area, which presumably leads to the observed increase in device efficiency.

The surfaces of the fumigated films were also analysed by SEM (Figure 4). The SEM image of the f-$MAPbI_3$ film shows good coverage and a clear grain morphology (the size ranges from 100-280 nm, Figure 4a). The SEM image of the f-$IM_{0.1}MA_{0.9}PbI_3$ film reveals a larger grain size compared to that of the reference material (Figure 4b), and as the dopant concentration increases, the grain size increases correspondingly. However, it is worth mentioning that there appears to be an amorphous substance attached to the film, which increases as the IMI content is increased. In the f-$IM_{0.2}MA_{0.8}PbI_3$ and f-$IM_{0.3}MA_{0.7}PbI_3$ films, where the IMI content highest, this amorphous substance appears to be separated between crystals, which is not conducive to electronic transmission (Figures 4c and 4d).

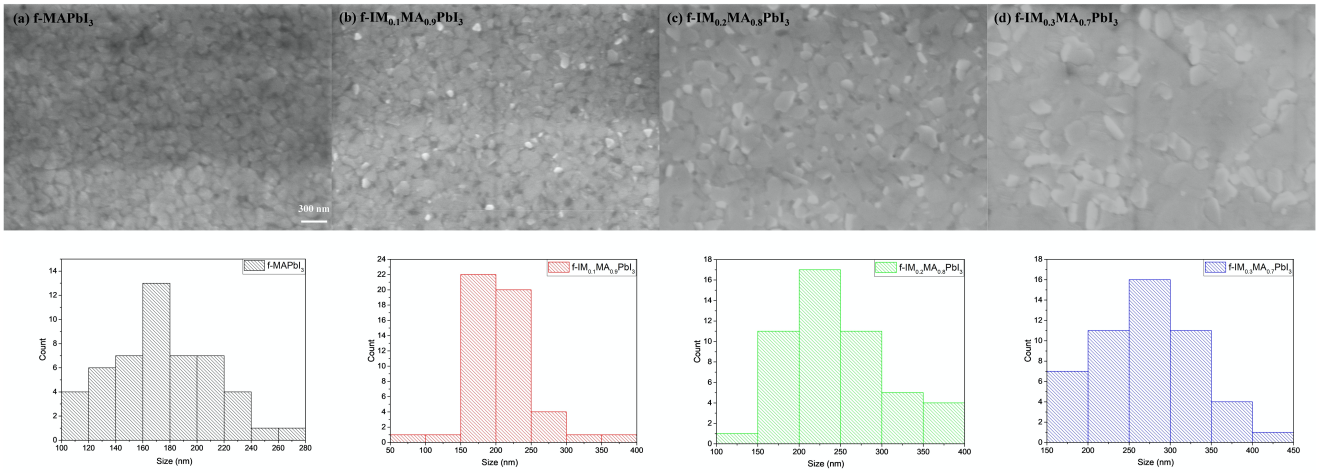

Figure 4. Morphological analysis of the fumigated films (a) f-$MAPbI_3$, (b) f-$IM_{0.1}MA_{0.9}PbI_3$, (c) f-$IM_{0.2}MA_{0.8}PbI_3$ and (d) f-$IM_{0.3}MA_{0.7}PbI_3$ after 20 min annealing at 100°C. Top-view SEM images of perovskite films after 20 min annealing at 100°C (top). Grain size distributions estimated from the SEM images using Nano measurer 1.2 software (bottom).

PSCs were fabricated from the fumigated films and the *J–V* characteristics of the devices under simulated air mass 1.5 global standard sunlight (AM 1.5 G) are summarized in Figure 5a with the device parameters listed in Table 1.

Table 1. Photovoltaic parameters J_{sc}, V_{oc}, FF and PCE with reverse scan of f-$IM_{0.1}MA_{0.9}PbI_3$, f-$IMD_{0.1}MA_{1.0}PbI_3$, f-$IM_{0.2}MA_{0.8}PbI_3$ and f-$IM_{0.3}MA_{0.7}PbI_3$ and f-$MAPbI_3$ champion devices.

Sample	J_{sc} (mA cm^{-2})	V_{oc} (V)	FF	PCE (%)
f-$MAPbI_3$	22.18	1.06	0.775	18.22
f-$IM_{0.1}MA_{0.9}PbI_3$	22.88	1.11	0.793	20.13

f-$IMD_{0.1}MA_{1.0}PbI_3$	22.36	1.08	0.777	18.74
f-$IM_{0.2}MA_{0.8}PbI_3$	21.56	1.09	0.778	18.21
f-$IM_{0.3}MA_{0.7}PbI_3$	21.82	1.06	0.766	17.72

Champion devices of the f-$MAPbI_3$ shows a PCE of 18.22%, obtained from the reverse scanned data of J_{SC} = 22.18 mA cm^{-2}, V_{OC} = 1.06 V and FF = 0.775. The most efficient f-$IM_{0.1}MA_{0.9}PbI_3$-based device provides a PCE of 20.13%, due to the auto-passivation of crystal defects by IMD, significantly outperforming that based on the f-$MAPbI_3$ reference material. However, in the devices prepared with fumigated films prepared using higher amounts of IMI, i.e. f-$IM_{0.2}MA_{0.8}PbI_3$ and f-$IM_{0.3}MA_{0.7}PbI_3$, the PCE is 18.21 and 17.72%, respectively. The PCE of the champion device made with the IMD doped film, f-$IMD_{0.1}MA_{1.0}PbI_3$, is 18.74%, significantly lower than the PCE of 20.13% obtained from the champion device containing f-$IM_{0.1}MA_{0.9}PbI_3$. The performance of the corresponding devices prepared under the anti-solvent method is provided in Figure S4 and Table S6, and are all lower than the devices containing the fumigated perovskite films. This provides statistical relevance to the results, confirming that the improvement of device performance is not due to IMI doping alone. An evaluation of the *J-V* hysteresis based on the scan direction was conducted (Figure 5b and Table S5) and, compared to the reference f-$MAPbI_3$ device, a similar hysteresis is observed for the f-$IM_{0.1}MA_{0.9}PbI_3$ device. This may be reflected in the hysteresis index,[30] which is calculated from the ratio between η_{Rev}/η_{For}. The hysteresis index of the reference f-$MAPbI_3$-based cells and f-$IM_{0.1}MA_{0.9}PbI_3$ devices are calculated as 1.03 and 1.05. Moreover, the high J_{SC} of 22.88 mA cm^{-2} obtained using the f-$IM_{0.1}MA_{0.9}PbI_3$ device is markedly better than that of the reference cell. In addition, the f-$IM_{0.1}MA_{0.9}PbI_3$ device exhibits a higher incident photon-to-current efficiency (IPCE) as a function of wavelength with a very broad plateau of over 80% between 400 and 725 nm, yielding an integrated J_{SC} value of 22.32 mA cm^{-2}, which is in good agreement with that determined from the *J-V* curves (Figure 5c).

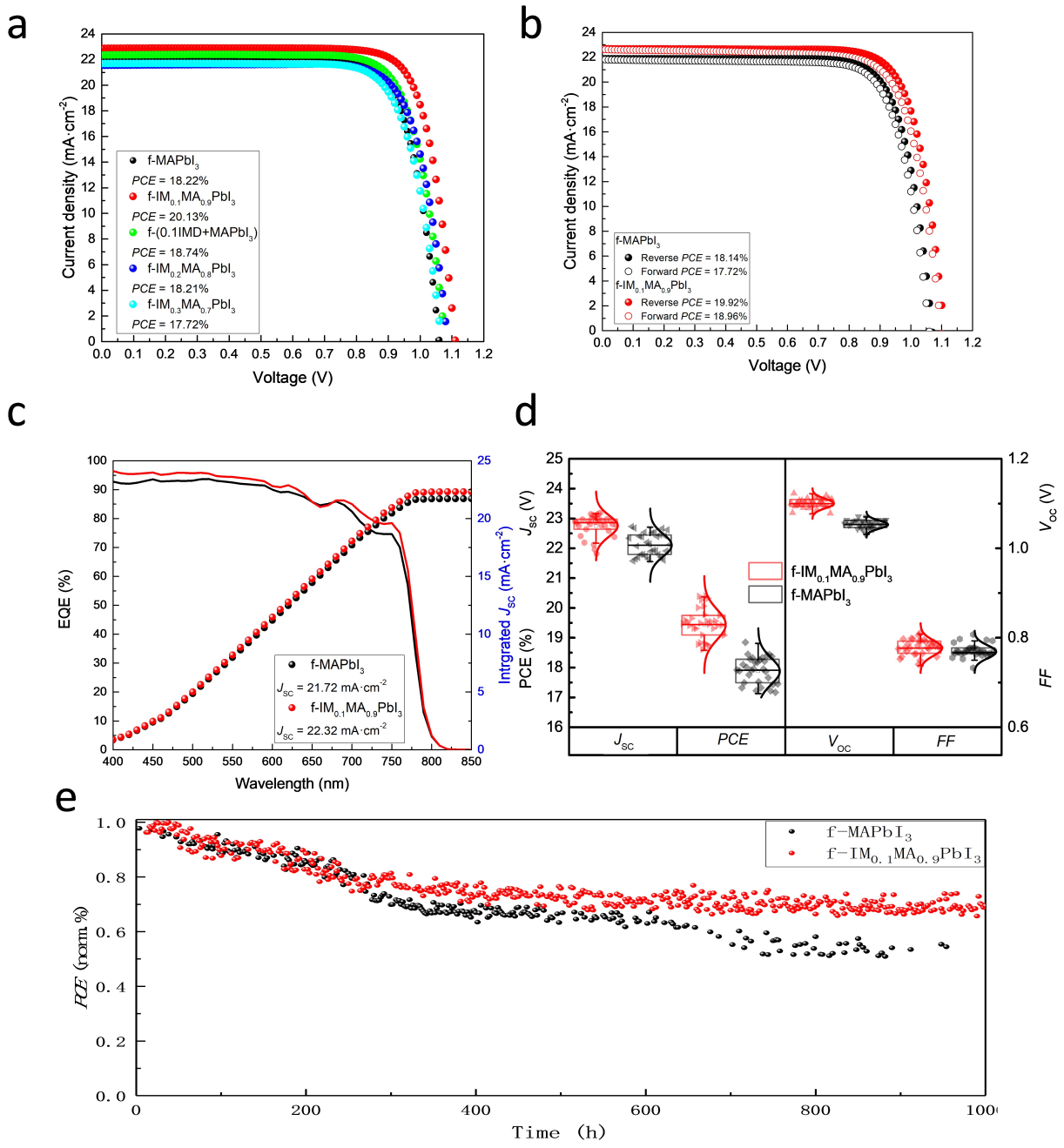

Figure 5. (a) The *J-V* characteristics of the f-$MAPbI_3$, f-$IM_{0.1}MA_{0.9}PbI_3$, f-$IMD_{0.1}MA_{1.0}PbI_3$, f-$IM_{0.2}MA_{0.8}PbI_3$ and f-$IM_{0.3}MA_{0.7}PbI_3$ champion devices, (b) hysteresis analysis, (c) IPCE of the f-$MAPbI_3$ and f-$IM_{0.1}MA_{0.9}PbI_3$ devices at a scan rate of 50 mV/s and (d) statistical deviation of the photovoltaic parameters (30 different solar cells each) based on the f-$MAPbI_3$ and f-$IM_{0.1}MA_{0.9}PbI_3$ devices measured under 100 mW cm^{-2} photon flux (AM 1.5G). (e) Stability study shown as in situ measured PCE of unsealed f-$IM_{0.1}MA_{0.9}PbI_3$ solar cell over 1000 hours under Ar.

A total of 60 solar cells were fabricated with the f-$IM_{0.1}MA_{0.9}PbI_3$ and f-$MAPbI_3$ films. Figure 5d shows the statistical distribution of all four photovoltaic parameters of the two groups of solar cells illustrating the reproducibility of each condition. In the case of the PSCs containing the f-$IM_{0.1}MA_{0.9}PbI_3$ films, the average values (with standard deviation, s.d.) of the short-circuit current

density (J_{SC}), open-circuit voltage (V_{OC}), fill factor (FF) and PCE are 22.75 ± 0.36 mA cm^{-2}, 1.1 ± 0.01 V, 0.78 ± 0.02 and 19.44 ± 0.51%, respectively (Table S3, SI). Compared to the f-$IM_{0.1}MA_{0.9}PbI_3$-containing cells, a smaller PCE of 17.88 ± 0.45% was obtained for the f-$MAPbI_3$-based devices (as well as a J_{SC} of 22.1 ± 0.38 mA cm^{-2}, V_{OC} of 1.05 ± 0.01 V and FF of 0.77 ± 0.01). As can be seen in Figure 5d, all the photovoltaic parameters of the f-$IM_{0.1}MA_{0.9}PbI_3$-based solar cells showed higher average values and smaller standard deviation (except FF) over those of devices containing the f-$MAPbI_3$ films (Table S4, SI). The stability of devices containing the f-$IM_{0.1}MA_{0.9}PbI_3$ solar cell was evaluated at the maximum power output (MPO) decay of the devices. The unsealed devices were maintained in an argon atmosphere under a constant illumination of 100 mW cm^{-2}. The current-voltage curves were recorded every 2 hours and the f-$IM_{0.1}MA_{0.9}PbI_3$ was found to be very stable (Figure 5e), as shown in the fitted decay lifetime. The performance of device decreased slowly during the aging study and after 1000 hours of continuous light soaking the MPO values of the devices kept more than 70% of the initial values, which is significantly better than the pure f- $MAPbI_3$.

Concluding remarks

Several routes to engineering the hybrid perovskites have been reported, such as cation alloying and halide alloying. However, most of the alloying approaches are limited to the well-studied, 3-dimensional perovskites such as $MAPbI_3$ and $FAPbI_3$. In this study, using IMI at a high doping level, combined with passivation using methylamine gas, affords a high-quality perovskite film delivering in a champion PSC a PCE of 20.14% and remarkable stability. The mechanism by which the structure of the film is improved involves deprotonation of the imidazolium to affording MA and IMD. The imidazole is then replaced by the newly generated MA cations resulting in a type of melting/freezing process that improves the quality of the film. Overall, this work shows that classical perovskite materials can potentially be doped with many different organic cations. In addition to the size of the cation being important, the pK_b should be below that of methylamine to ensure that in the fumigation step the organic cation can be deprotonated.

Acknowledgement: We thank CTI 25590.1 PFNM-NM, Solaronix, Aubonne, Switzerland, EPFL and Swiss National Science Foundation for financial support and Borun New Material Technology for providing high quality Spiro-OMeTAD. G. G. acknowledges the Swiss National Science Foundation (SNSF) funding through the Ambizione Energy project HYPER (grant number PZENP2_173641)

References

1 Kojima, A.; Teshima, K.; Shirai, Y.; Miyasaka, T. Organometal Halide Perovskites as Visible-Light

Sensitizers for Photovoltaic Cells. *J. Am. Chem. Soc.* **2009**, *131*, 6050-6051.

2 Collavini, S.; Völker, S. F.; Delgado, J. L. Understanding the Outstanding Power Conversion Efficiency of Perovskite-Based Solar Cells. *Angew. Chem. Int. Ed.* **2015**, *54*, 9757-9759.

3 Gao, P.; Grätzel, M.; Nazeeruddin, M. K. Organohalide lead perovskites for photovoltaic applications. *Energy Environ. Sci.* **2014**, *7*, 2448-2463.

4 Yang, S.; Fu, W.; Zhang, Z.; Chen, H.; Li, C.-Z. Recent advances in perovskite solar cells: efficiency, stability and lead-free perovskite, *J. Mater. Chem. A*, **2017**, *5*, 11462-11482.

5 Eperon, G. E.; Stranks, S. D.; Menelaou, C.; Johnston, M. B.; Herz, L. M.; Snaith, H. J. Formamidinium lead trihalide: a broadly tunable perovskite for efficient planar heterojunction solar cells. *Energy Environ. Sci.* **2014**, *7*, 982-988.

6 Lee, J.-W.; Lee, S. H.; Ko, H.-S.; Kwon, J.; Park, J. H.; Kang, S. M.; Ahn, N.; Choi, M.; Kim, J. K.; Park, N.-G. Opto-electronic properties of TiO_2 nanohelices with embedded $HC(NH_2)_2PbI_3$ perovskite solar cells. *J. Mater. Chem. A*, **2015**, *3*, 9179-9186.

7 Aharon, S.; Dymshits, A.; Rotem, A.; Etgar, L. Temperature dependence of hole conductor free formamidinium lead iodide perovskite based solar cells. *J. Mater. Chem. A*, **2015**, *3*, 9171-9178.

8 Koh, T. M.; Fu, K.; Fang, Y.; Chen, S.; Sum, T. C.; Mathews, N.; Mhaisalkar, S. G.; Boix, P. P.; Baikie, T. Formamidinium-Containing Metal-Halide: An Alternative Material for Near-IR Absorption Perovskite Solar Cells. *J. Phys. Chem. C* **2014**, *118*, 16458-16462.

9 Saliba, M.; Matsui, T.; Domanski, K.; Seo, J. Y.; Ummadisingu, A.; Zakeeruddin, S. M.; Correa-Baena, J. P.; Tress, W. R.; Abate, A.; Hagfeldt, A.; Grätzel, M.; Incorporation of rubidium cations into perovskite solar cells improves photovoltaic performance. *Science* **2017**, *355*, 722-726.

10 Ma, T.; Zhang, Q.; Tadaki, D.; Hirano-Iwata, A.; Niwano, M. Fabrication and Characterization of High-Quality Perovskite Films with Large Crystal Grains. *J. Phys. Chem. Lett.* **2017**, *8*, 720-726.

11 Bi, D.; Tress, W.; Dar, M. I.; Gao, P.; Luo, J.; Renevier, C.; Schenk, K.; Abate, A.; Giordano, F., Correa Baena, J.-P., Decoppet, J.-D.; Zakeeruddin, S. M.; Nazeeruddin, M. K.; Grätzel, M.; Hagfeldt, A. Efficient luminescent solar cells based on tailored mixed-cation perovskites. *Sci. Adv.* **2016**, 2, e1501170.

12 Mahmood, K.; Sarwar, S.; Mehran, M. T. Current status of electron transport layers in perovskite solar cells: materials and properties. *RSC Adv.* **2017**, *7*, 17044-17062.

13 Yang, G.; Tao, H.; Qin, P.; Ke, W.; Fang, G. Recent progress in electron transport layers for efficient perovskite solar cells. *J. Mater. Chem. A*. **2016**, *4*, 3970-3990.

14Moriya M.; Hirotani, D.; Ohta, T.; Ogomi, Y.; Shen, Q.; Ripolles, T. S.; Yoshino, K.; Toyoda, T.; Minemoto, T.; Hayase, S. Architecture of the Interface between the Perovskite and Hole-Transport Layers in Perovskite Solar Cells. *ChemSusChem* **2016**, *9*, 2634-2639.

15 Calil, L.; Kazim, S.; Grätzel, M.; Ahmad, S. Hole-Transport Materials for Perovskite Solar Cells.

Angew. Chem. Int. Ed. **2016**, *55*, 14522-14545.

16 Kim, Y. C.; Jeon, N. J.; Noh, J. H.; Yang, W. S.; Seo, J.; Yun, J. S.; Ho-Baillie, A.; Huang, S.; Green, M. A.; Seidel, J.; Ahn, T. K.; Seok, S. Il. Beneficial Effects of PbI2 Incorporated in Organo‐Lead Halide Perovskite Solar Cells. *Adv. Energy Mater.* **2016**, *6*, 1502104.

17 Zheng, X.; Chen, B.; Dai, J.; Fang, Y.; Bai, Y.; Lin, Y.; Wei, H.; Zeng, X. C.; Huang, J. Defect passivation in hybrid perovskite solar cells using quaternary ammonium halide anions and cations. *Nat. Energy*, **2017**, *2*, 17102.

18 Noel, N. K.; Abate, A.; Stranks, S. D.; Parrott, E. S.; Burlakov, V. M.; Goriely, A.; Snaith, H. J. Enhanced Photoluminescence and Solar Cell Performance via Lewis Base Passivation of Organic–Inorganic Lead Halide Perovskites. *ACS Nano*, **2016**, *8*, 9815-9821.

19 Abate, A.; Saliba, M.; Hollman, D. J.; Stranks, S. D.; Wojciechowski, K.; Avolio, R.; Grancini, G.; Petrozza, A.; Snaith, H. J. Supramolecular Halogen Bond Passivation of Organic–Inorganic Halide Perovskite Solar Cells. *Nano Lett.* **2014**, *14*, 3247-3254.

20 Tripathi, N.; Shirai, Y.; Yanagida, M.; Karen, A.; Miyano, K. Novel Surface Passivation Technique for Low-Temperature Solution-Processed Perovskite PV Cells. *ACS Appl. Mater. Interfaces*, **2016**, *8*, 4644-4650.

21 Tan, H.; Jain, A.; Voznyy, O.; Lan, X.; García de Arquer, F. P.; Fan, J. Z.; Quintero-Bermudez, R.; Yuan, M.; Zhang, B.; Zhao, Y.; Fan, F.; Li, P.; Quan, L. N.; Zhao, Y.; Lu, Z. H.; Yang, Z.; Hoogland, S.; Sargent, E. H. Efficient and stable solution-processed planar perovskite solar cells via contact passivation. *Science* **2017**, *355*, 722-726.

22 Zhang, C.-C.; Li, M.; Wang, Z.-K.; Jiang, Y.-R.; Liu, H.-R.; Yang, Y.-G.; Gao, X.-Y.; Ma, H. Passivated perovskite crystallization and stability in organic–inorganic halide solar cells by doping a donor polymer. *J. Mater. Chem. A*, **2017**, *5*, 2572-2579.

23 Lee, Y.; Paek, S.; Cho, K. T.; Oveisi, E.; Gao, P.; Lee, S.; Park, J.-S.; Zhang, Y.; Humphry-Baker, R.; Asirid, A. M.; Nazeeruddin, M. K. Enhanced charge collection with passivation of the tin oxide layer in planar perovskite solar cells. *J. Mater. Chem. A*, **2017**, *5*, 12729-12734.

24 Heo, S.; Seo, G., Leec, Y.; Lee, D.; Seol, M.; Lee, J.; Park, J.-B.; Kim, K.; Yun, D.-J.; Kim, Y. S.; Shin, J. K.; Ahn, T. K.; Nazeeruddin, M. K. Deep level trapped defect analysis in $CH_3NH_3PbI_3$ perovskite solar cells by deep level transient spectroscopy. *Energy Environ. Sci.* **2017**, *10*, 1128-1133.

25 Ball, J. M.; Petrozza, A. Defects in perovskite-halides and their effects in solar cells. *Nat. Energy*, **2016**, *1*, 16149.

26 Zhou, Z. ; Wang, Z. ; Zhou, Y.; Pang, S.; Wang, D.; Xu, H. ; Liu, Z.; Padture, N. P.; Cui, G. *Angew. Chem. Int. Ed*. **2015**, *54*, 9705-9709.

27 Clayden, J.; Greeves, N.; Warren, S. *Organic Chemistry*, Oxford University, Press, Oxford, UK **2012**.

28 Bordwell, F. G. Equilibrium acidities in dimethyl sulfoxide solution. *Acc. Chem. Res*. **1988**, *21*, 456-463.

29 Stoumpos, C. C.; Malliakas, C. D.; Kanatzidis, M. G. Semiconducting Tin and Lead Iodide Perovskites with Organic Cations: Phase Transitions, High Mobilities, and Near-Infrared Photoluminescent Properties. *Inorg. Chem*. **2013**, *52*, 9019-9038.

30 Pellet, N.; Gao, P.; Gregori, G.; Yang, T.-Y.; Nazeeruddin, M. K.; Maier, J.; Grätzel, M. Mixed-Organic-Cation Perovskite Photovoltaics for Enhanced Solar-Light Harvesting. *Angew. Chem. Int. Ed*. **2014**, *53*, 3151-3157.

31 Huang, Y.; Li, L.; Liu, Z.; Jiao, H.; He, Y.; Wang, X.; Zhu, R.; Wang, D.; Sun, J.; Chen, Q.; Zhou, H. The intrinsic properties of $FA_{(1-x)}MA_xPbI_3$ perovskite single crystals. *J. Mater. Chem. A,* **2017**, *5*, 8537-8544.

32 Safdari, M.; Fischer, A.; Xu, B.; Kloo, L.; Gardner, J. M. Structure and function relationships in alkylammonium lead(II) iodide solar cells. *J. Mater. Chem. A*, **2015**, *3*, 9201-9207.

33 Kieslich, G.; Sun, S.; Cheetham, A. K. Solid-state principles applied to organic–inorganic perovskites: new tricks for an old dog. *Chem. Sci*. **2014**, 5, 4712-4715.

34 Glazer, A. M. The Classification of Tilted Octahedra in Perovskite. *Acta Crystallogr., Sect. B: Struct. Crystallogr. Cryst. Chem.* **1972**, *28*, 3384-3392.

35 Jodlowski, A. D.; Roldán-Carmona, C.; Grancini, G.; Salado, M.; Ralaiarisoa, M.; Ahmad, S.; Koch, N.; Camacho, L.; Miguel G.; Nazeeruddin M. K.; Large guanidinium cation mixed with methylammonium in lead iodide perovskites for 19% efficient solar cells. *Nature Energ.* **2017**, *2*, 972–979.

36 Weller, M. T.; Weber, O. J.; Frost, J. M.; Walsh, A. Cubic Perovskite Structure of Black Formamidinium Lead Iodide, α-$[HC(NH_2)_2]PbI_3$, at 298 K. *J. Phys. Chem. Lett*. **2015**, *6*, 3209-3212.

37 Weclawik, M.; Gagor, A.; Piecha, A.; Jakubas, R.; Medycki, W. Synthesis, crystal structure and phase transitions of a series of imidazolium iodides. *CrystEngComm* **2013**, *15*, 5633-5640.

38 Weber, O. J.; Marshall, K. L.; Dyson, L. M.; Weller, M. T. Structural diversity in hybrid organic–inorganic lead iodide materials, *Acta Crystallogr. Sect. B*, **2015**, *71*, 668-678.

39 Zhang, Y.; Grancini, G.; Feng, Y.; Asiri, A. M.; Nazeeruddin, M. K. Optimization of Photostable Quasi-Cubic $FA_xMA_{1-x}PbI_3$ Perovskite Structure for Solar Cells with Efficiency beyond 20%. *ACS Energy Lett.* **2017**, *2*, 802-806.

40 Travis, W.; Glover, E. N. K.; Bronstein, H.; Scanlonbc, D. O.; Palgrave, R. G. On the application of the tolerance factor to inorganic and hybrid halide perovskites: a revised system, *Chem. Sci*., **2016**, *7*, 4548-4556.

41 Li, Z.; Yang, M.; Park, J.-S.; Wei, S.-H. ; Berry, J. J.; Zhu, K. Stabilizing Perovskite Structures by Tuning Tolerance Factor: Formation of Formamidinium and Cesium Lead Iodide Solid-State Alloys,

Chem. Mater., **2016**, *28*, 284-292.

42 Stoumpos, C. C.; Malliakas, C. D.; Kanatzidis, M. G. Semiconducting Tin and Lead Iodide Perovskites with Organic Cations: Phase Transitions, High Mobilities, and Near-Infrared Photoluminescent Properties. *Inorg. Chem*. **2013**, *52*, 9019-9038.

43 Pellet, N.; Gao, P.; Gregori, G.; Yang, T.-Y.; Nazeeruddin, M. K.; Maier, J.; Grätzel, M. Mixed-Organic-Cation Perovskite Photovoltaics for Enhanced Solar-Light Harvesting. *Angew. Chem. Int. Ed*. **2014**, *53*, 3151-3157.

44 Huang, Y.; Li, L.; Liu, Z.; Jiao, H.; He, Y.; Wang, X.; Zhu, R.; Wang, D.; Sun, J.; Chen, Q.; Zhou, H. The intrinsic properties of $FA_{(1-x)}MA_xPbI_3$ perovskite single crystals. *J. Mater. Chem. A,* **2017**, *5*, 8537-8544.

45 Peng, W.; Miao, X.; Adinolfi, V.; Alarousu, E.; Tall, O. E.; Emwas, A.-H.; Zhao, C.; Walters, G. ; Liu, J.; Ouellette, O.; Pan, J.; Murali, B.; Sargent, E. H.; Mohammed, O. F.; Bakr, O. M. Engineering of $CH_3NH_3PbI_3$ Perovskite Crystals by Alloying Large Organic Cations for Enhanced Thermal Stability and Transport Properties. *Angew. Chem. Int. Ed*. **2016**, *55*, 10686-10690.

46 Maughan, A. E.; Kurzman, J. A.; Neilson, J. R. Hybrid Inorganic-Organic Materials with an Optoelectronically Active Aromatic Cation: $(C_7H_7)_2SnI_6$ and $C_7H_7PbI_3$. *Inorg. Chem.* **2015**, *54*, 370-378.

47 Kamminga, M. E.; Fang, H.-H.; Filip, M. R.; Giustino, F.; Baas, J.; Blake, G. R.; Loi, M. A.; Palstra, T. T. M. Confinement Effects in Low-Dimensional Lead Iodide Perovskite Hybrids, *Chem. Mater.* **2016**, *28*, 4554-4562.

48 Zhang, Y.; Fei, Z.; Gao, P.; Lee, Y.; Tirani, F. F.; Scopelliti, R.; Feng, Y.; Dyson, P. J.; Nazeeruddin, M. K. A Strategy to Produce High Efficiency, High Stability Perovskite Solar Cells Using Functionalized Ionic Liquid-Dopants. *Adv. Mater*. **2017**, 29, 1702157.

49 Grancini, G.; Marras, S.; Prato, M.; Giannini, C.; Quarti, C.; De Angelis, F.; De Bastiani, M.; Eperon, G. E.; Snaith. H. J.; Manna, L.; Petrozza, A. The Impact of the Crystallization Processes on the Structural and Optical Properties of Hybrid Perovskite Films for Photovoltaics. *J. Phys. Chem. Lett.*, **2014**, 5, 3836–3842.

50 Bastiani, M.; D'Innocenzo V.; Stranks, S. D.; Snaith, H. J.; Petrozza, A. Role of the crystallization substrate on the photoluminescence properties of organo-lead mixed halides perovskites. *APL Mater.,* **2014**, 2, 081509.

51 Stranks, S. D.; Burlakov, V. M.; Leijtens, T.; Ball, J. M.; Goriely, A.; Snaith, H. J. Recombination Kinetics in Organic-Inorganic Perovskites: Excitons, Free Charge, and Subgap States, *Phys. Rev. Appl.* **2014**, *2*, 034007.

52 Zhang, Y.; Gao, P.; Oveisi, E.; Lee, Y.; Jeangros, Q.; Grancini, G.; Paek, S., Feng, Y.; Nazeeruddin, M. K. PbI_2−HMPA Complex Pretreatment for Highly Reproducible and Efficient $CH_3NH_3PbI_3$

Perovskite Solar Cells, *J. Am. Chem. Soc.* **2016**, *138*, 14380-14387.

53 Yang, Y.; Yang, M.; Moore, D. T.; Yan, Y.; Miller, E. M.; Zhu, K.; Beard, M. C. Top and bottom surfaces limit carrier lifetime in lead iodide perovskite films. *Nat. Energy* **2017**, *2*, 16207.

54 Yang, M.; Zeng, Y.; Li, Z.; Kim, D. H.; Jiang, C.-S.; van de Lagemaat, J.; Zhu, K. Do grain boundaries dominate non-radiative recombination in $CH_3NH_3PbI_3$ perovskite thin films? *Phys. Chem. Chem. Phys.* **2017**, *19*, 5043-5050.

55 Conings, B.; Bretschneider, S. A.; Babayigit, A.; Gauquelin, N.; Cardinaletti, I.; Manca, J.; Verbeeck, J.; Snaith, H. J.; Boyen, H.-G. Structure–Property Relations of Methylamine Vapor Treated Hybrid Perovskite $CH_3NH_3PbI_3$ Films and Solar Cells. *ACS Appl. Mater. Interfaces* **2017**, *9*, 8092-8099.